

Adaptive actin organization buffers endocytosis against changes in membrane tension

Charlotte Kaplan¹, Sam J. Kenny², Shirley Chen², Johannes Schöneberg¹, Ewa Sitarska^{3,§}, Alba Diz-Muñoz³, Matthew Akamatsu^{1*}, Ke Xu^{2,4*} and David G. Drubin^{1*}

¹Department of Molecular and Cell Biology, University of California, Berkeley, CA 94720-3220

²Department of Chemistry, University of California, Berkeley, CA 94720-3220

³Cell Biology and Biophysics Unit, European Molecular Biology Laboratory Heidelberg, Meyerhofstrasse 1, 69117 Heidelberg

⁴Chan Zuckerberg Biohub, San Francisco, CA 94158.

§ Collaboration for joint PhD degree between EMBL and Heidelberg University, Faculty of Biosciences

*Correspondence to DGD (drubin@berkeley.edu (510-642-0940) MA (matt.akamatsu@berkeley.edu) or KX (xuk@berkeley.edu)

Preprint Server

Two versions of this manuscript have been uploaded to bioRxiv:
<https://www.biorxiv.org/content/10.1101/2020.04.05.026559v1>

Classification

Cell biology

Keywords

Clathrin-mediated endocytosis; actin; membrane tension; super-resolution microscopy

Author contributions

C. Kaplan and D.G. Drubin conceived the study and experiments. C. Kaplan performed live cell data acquisition, SRM data analysis and live cell data analysis. S. J. Kenny, S. Chen and K. Xu performed SRM, super-resolution data reconstruction and supervised SRM imaging. J. Schöneberg supported the SRM data analysis. E. M. Sitarska and A. Diz-Muñoz performed membrane tether pulling experiments by atomic force microscopy, data analysis and supervised AFM tether pulling experiments. C. Kaplan, and M. Akamatsu prepared the plot layouts and figures. C. Kaplan, M. Akamatsu, and D.G. Drubin wrote the manuscript with feedback from the other authors.

This PDF file includes:

Main Text

Figures 1 to 4

Significance Statement

The actin cytoskeleton ensures robustness of clathrin-mediated endocytosis in the face of changes in mechanical resistance in the form of membrane tension. However, how the actin cytoskeleton adapts to changes in mechanical resistance during endocytosis was not known. Computer simulations and reconstituted systems predict that actin network architecture and filament density can adapt to changes in resistance, but evidence for such an adaptive mechanism in cells has been lacking. Here, two-color, 3D super-resolution microscopy and live-cell fluorescence microscopy showed that under elevated membrane tension, the actin network increases its size and coverage around clathrin-coated pits in a manner conducive to additional force production. The network grows from the base of the pit, implying that it generates a pulling force.

Abstract (250 words), 235 words

Clathrin-mediated endocytosis (CME) remains robust despite variation in plasma membrane tension. Actin assembly-mediated force generation becomes essential for CME under high membrane tension, but the compensatory mechanisms are not understood. We investigated actin network ultrastructure at the shallow, “U” and “Ω” morphological stages of clathrin-coated pit formation using super-resolution microscopy, which allowed large numbers of pits to be quantitatively examined in an unbiased manner. The spatial organization of actin and the Arp2/3 complex activator N-WASP, a polymerization regulator, indicate that actin polymerization initiates at the base of clathrin-coated pits and that the actin network then grows away from the plasma membrane. Surprisingly, actin network growth is not tightly coupled to endocytic clathrin coat shape. We tested whether membrane tension-dependent changes in actin assembly might explain this uncoupling. Under elevated membrane tension, CME slows down and the actin network grows higher, resulting in greater coverage of the clathrin coat. When we inhibited actin polymerization with CK666, a small molecule Arp2/3 complex inhibitor, under elevated membrane tension, we found that shallow clathrin-coated pits accumulated, indicating that this adaptive mechanism is especially crucial during the initial membrane curvature-generating stages of CME. Our findings reveal that adaptive force generation by the actin network ensures that CME remains robust over a range of plasma membrane tension regimes. Given that actin assembly mediates many membrane remodeling events, we expect that adaptive actin assembly will be a common feature of such systems.

Introduction

From yeast to humans, transient actin assembly is associated with the formation of clathrin-coated endocytic vesicles. In yeast cells, actin assembly is required to generate forces to invaginate the plasma membrane against a high intrinsic turgor pressure for CME (1–4). In mammalian cells, actin assembly augments CME and becomes increasingly critical as plasma membrane tension increases (5–7). When actin assembly is perturbed in mammalian cells, CME typically slows in a manner that depends on cell type (7–10). A potential cause of this reported variation between cell types might be differences in plasma membrane tension (11, 12). Actin perturbation results in the accumulation of “U-shaped” membrane invaginations, reflecting difficulty in progressing to the subsequent “ Ω -shaped” membrane stage (5, 8, 13, 14). These findings suggest that in general actin assembly improves the efficiency of CME in mammalian cells, potentially compensating for changes in plasma membrane tension.

Despite the fact that actin assembly appears to be associated with CME in all eukaryotes and over a large range of membrane tension values, how the actin cytoskeleton produces force and whether it adapts to changes in membrane tension are not known. *In vitro* and *in silico* studies suggest that actin networks can adapt their architecture in response to force, but evidence for this adaptive mechanism in cells is limited (15–17). Knowing whether the actin cytoskeleton at CME sites adapts to changes in membrane tension will facilitate elucidation of the fundamental mechanisms by which cytoskeletal complexes produce force in the mechanically varying environment of cells. Platinum replica electron microscopy of cultured cells led to the proposal that actin networks assemble in a collar-like arrangement around the vesicle neck (18). This actin organization would imply that a constricting force is generated toward the neck of the pit, supporting fission. However, actin filaments interact not only with the vesicle neck, but also with

the bud surface, given that the clathrin coat is impregnated with actin-binding linker proteins like Hip1R and Epsin (19–22). Such an arrangement would imply that actin filaments also apply a force that pulls the clathrin-coated pit into the cell interior (17).

In yeast, such a pulling mechanism is likely. Actin filaments are nucleated in a ring surrounding the pit, and the resulting filaments are coupled to the clathrin coat surface, generating an inward force orthogonal to the plane of the plasma membrane (1, 23–27). Because the endocytic machinery is highly conserved from yeast to mammals, a similar mechanism for actin force generation during CME seems likely (17). However, ultrastructural evidence for actin organization through different stages of mammalian CME, and for how this organization might respond to changing membrane tension, are lacking.

Several competing models for actin organization at CME sites in mammalian cells have been proposed, so it is important to distinguish between these models (5, 19–22). Recent advances in super-resolution microscopy (SRM) permit examination of cellular ultrastructure with large sample sizes, low invasiveness and high molecular specificity to reveal the ultrastructure of membrane cytoskeletal systems in mammalian cells (28–30).

Here, we combined two-color, three-dimensional stochastic optical reconstruction microscopy (2c-3D STORM) and live-cell fluorescence imaging to determine how filamentous actin is organized at CME sites at different stages of internalization under varying values of plasma membrane tension. These measurements lead to the conclusion that the actin network grows from the base of the pit inward, supporting a pulling mechanism for mammalian endocytic actin filaments. The size of the actin network is not tightly coupled to the stage of CME progression. Importantly, under elevated membrane tension, the actin network grows larger around the pit, and appears to be required at an earlier CME stage. These observations support a mechanism in which

the actin network actively adapts to load by increasing in size and producing additional force to ensure robust CME across a wide range of values of membrane tension.

Results

Actin organization at CME sites suggests that force generation can be both parallel and orthogonal to the axis of clathrin-coated pit formation at different sites in the same cell

We used 2c-3D STORM to determine the ultrastructural organization of the actin cytoskeleton at sites of clathrin-mediated endocytosis. Henceforth, we refer to clathrin-coated structures (CCSs) as relatively flat clathrin structures and clathrin-coated pits (CCPs) as curved, invaginating clathrin structures. Our 2c-3D STORM method preserves cellular ultrastructure by chemical fixation of intact cells, provides high molecular specificity due to immunofluorescence labeling, and allows large numbers of sites to be imaged (28). We conducted our experiments on a skin-melanoma cell line (SK-MEL-2) wherein ~87% of dynamin2-eGFP^{EN} (DNM2-eGFP^{EN}) spots co-accumulate with actin (7). We used this SK-MEL-2 cell line endogenously expressing DNM2-eGFP^{EN} and clathrin light chain A-tagRFP-T (CLTA-TagRFP-T^{EN}) for both live-cell and super-resolution experiments (31).

In these cells, we resolved CF680-labeled CCSs as discrete, round or elliptical shapes on the ventral surface (Fig. 1A). The majority of the CCSs appeared connected to filamentous actin visualized by Alexa Fluor 647-tagged phalloidin. These super-resolution reconstructions resolve the association between clathrin coats and actin networks for thousands of pits with high (10s of nm) resolution.

Knowing how actin networks are organized spatially in three dimensions at CME sites provides insights into its force generation mechanisms. We rendered the CCSs in three dimensions by cropping an area around each clathrin and actin structure to generate x-y and x-z STORM image

projections (Fig. 1B and C). To our surprise, we observed strikingly different actin filament spatial organizations in the clathrin coats we examined, even when they were near each other in the same cell and even when they are at the same morphological stage of CME (see below) (Fig. 1B). In the first example shown, a thin layer of actin filaments resided along the base of the clathrin coat (Fig. 1C, inset 1), reminiscent of structures observed in EM by Collins *et al.* (18). In contrast, in the second example, actin filaments covered the CCP completely (Fig. 1C, inset 2). This organization resembles actin interacting with the entire clathrin coat as in yeast (4, 27, 32–34) and recent cryo-electron tomograms (17). These micrographs indicate that distinct CME-associated actin structures can coexist in the same cell, consistent with models for force generation parallel to and orthogonal to the invagination axis.

CME site-associated actin networks grow from the CCP base to the tip of the coat and their organization is not coupled to CME progression

We used quantitative analysis of these STORM reconstructions to determine how actin is organized at CME sites and how actin organization relates to progression through CME. We first determined when actin filaments become detectable at CCSs and CCPs over the course of endocytosis by selecting 992 high-resolution clathrin coats based on quality control criteria explained in the Materials and Methods (Fig. S1A). We detected actin associated with 74% of the clathrin coats, which is comparable to previous measurements that we have made of endocytic traces in live cells of dynamin2-GFP events associated with actin-RFP, given that our super-resolved images are snapshots of a time-lapse event (7).

To identify the stages of CME in which associated actin is detectable, we classified the coats by stage based on their shape, similar to earlier analyses of electron micrographs (35).

Clathrin coats were classified as shallow, U-shaped, or Ω -shaped based on their aspect ratio (which we call the shape index) (Figs. 1D, S1B and C). We found a surprisingly wide variety of actin organizations in each of the three CME stages (Fig. 1E and S1D). To quantify the relationship between actin organization and endocytic stage, the shape index of the coat was plotted as a function of the extent of actin covering clathrin. When the actin network is larger in size than the clathrin coat, we define this state as 100% coverage (see Materials and Methods, Fig. S1B). There was no significant correlation between actin/coat coverage and coat shape for any of the three stages of CME progression (Fig. 1F). We also observed a lateral mean displacement between the peak signals of clathrin and actin of 74 ± 42 nm, indicating an asymmetry in actin localization around the pits (13). This asymmetry value did not significantly change between CME stages (Fig. S1E and F). We conclude that irrespective of endocytic stage, some pits have a thin actin network at the base of the pit, others have an intermediate level of coverage around the clathrin coat, and others have actin completely covering the pit. This result suggests that actin can polymerize at all stages of CME membrane deformation: shallow, U-shaped, and Ω -shaped.

In our reconstructions, we observed that whenever actin only partially covers the clathrin coat, the network is always located at the base of the pit (Fig. 1E). This observation suggests that actin polymerization is nucleated at the base of the pit and that the network then grows inward around and over the tip of the clathrin coat. To test the generality of this observation, we calculated the difference in average axial (Z) position between the clathrin and actin signals for each site. We define this difference, D_z , such that negative D_z corresponds to actin residing nearer the base of the pit (Fig. 1G). To determine whether actin grows from the base or tip of the pit, we plotted D_z as a function of the extent of coverage between actin and the clathrin coat. Increasing values of D_z would indicate that the network grows from the base of the pit toward the cell interior (Fig. 1G).

Indeed, as a function of actin/coat coverage, D_z increased from negative values to near zero (Fig. 1H). We conclude that actin polymerization is initiated at the base of clathrin coats.

Given our finding that actin growth originates from the base of the pit, we next investigated the spatial distribution of the actin nucleation factor N-WASP at clathrin coats by 2c-3D STORM. Consistent with our conclusions about where actin assembly occurs at CCPs, N-WASP localized to the base of both early clathrin coats and late clathrin coats (Fig. S2A). More unexpectedly, at some CME sites, N-WASP covered the entire clathrin coat in early and late stages (Fig. S2B).

In summary, we conclude that actin polymerization is nucleated at the base of clathrin-coated pits and grows toward the coat's tip (Fig. 1I). Unexpectedly, actin nucleation is not coupled to the stage of CME progression. A possible explanation for the variety of actin organizations we observed associated with clathrin coats is that actin network organization responds to changes in membrane tension to adapt the magnitude and orientation of forces produced.

Dynamics of clathrin-mediated endocytosis slow down under elevated membrane tension

We next combined osmotic shock with live-cell fluorescence microscopy and 2c-3D STORM to determine how actin-mediated force generation contributes to clathrin-coated pit formation under elevated membrane tension (Fig. 2A). Previous EM studies identified a requirement for actin filaments at the “U” to “ Ω ” transition (5). However, for a mechanistic understanding, the quantitative relationship between membrane tension and endocytic dynamics must be elucidated (17). Our quantitative light microscopy-based analysis of a large number of sites at different CME stages provided the necessary sensitivity to detect effects throughout the process. We first needed to establish conditions under which CME dynamics are affected by elevated membrane tension in these cells.

To determine how membrane tension is affected by changes in media osmolarity, we performed membrane tether pulling experiments by atomic force microscopy (AFM) on SK-MEL-2 cells cultured under isotonic conditions and hypotonic conditions (75 mOsm) (Fig. 2B). In isotonic media, the force required to maintain a pulled membrane tether was 33.0 ± 7.4 pN. Under hypotonic conditions the tether force increased to 48.0 ± 17.1 pN (Fig. 2B). These measurements allowed us to quantitatively relate a given hypotonic environment in these cells to changes in membrane tension.

To decipher the relationship between CME dynamics and membrane tension, we used total internal reflection fluorescence (TIRF) microscopy to image SK-MEL-2 cells under isotonic and hypotonic conditions (Fig. 2C). CLTA-TagRFP-T^{EN} and DNM2-eGFP^{EN} fluorescence lifetimes were determined by single-particle tracking (36). In isotonic media most clathrin tracks were relatively short (47 ± 32 s) with a burst of DNM2-eGFP^{EN} signal at the end (DNM2 lifetime 39 ± 32 s) (Fig. 2C, Supp. movie 1, Table S1). Neither isotonic media nor exchange to slightly hypotonic 225 mOsm media noticeably affected DNM2-eGFP^{EN} and CLTA-TagRFP-T^{EN} lifetimes or CME initiation and completion rates (Fig. S3 A-D). Only 1 - 2% of these CLTA-TagRFP-T^{EN} and DNM2-eGFP^{EN} fluorescence tracks persisted over the entire 4.8 min movie in these conditions (Fig. S3 B and D).

Upon treatment with moderately hypotonic (150 mOsm) media for 10 min, CLTA-TagRFP-T^{EN} lifetime in cells increased by 20% (60 ± 53 s versus 49 ± 1 s) (Fig. S3E). This moderate treatment also had mild effects on the CME initiation rate (15 ± 5 s versus 25 ± 6 s), completion rate (11 ± 4 s versus 19 ± 6 s), and stalling rate (events that persist the entire length of our 4.8 min movies) (3 ± 1 % versus 0.8 ± 0.9 % (Fig. S3F).

Treatment of cells with more strongly hypotonic (75 mOsm) media dramatically perturbed CME dynamics. After 2 minutes in 75 mOsm hypotonic media, tracks elongated and very often lasted the entire duration of the 4.8 min movie (Fig. 2C, Supp. movie 2, Table S1). The mean lifetimes of CLTA-TagRFP-T^{EN} and DNM2-eGFP^{EN} tracks were 128 ± 112 s (Fig. 2D) and 125 ± 112 s, respectively (Fig. 2E). We also observed a substantial decrease in CME initiation rate ($103 \pm 1.5 \mu\text{m}^{-2} \text{min}^{-1}$ versus $22.2 \pm 3.5 \mu\text{m}^{-2} \text{min}^{-1}$), completion rate $5.3 \pm 1.7 \mu\text{m}^{-2} \text{min}^{-1}$ versus $17.8 \pm 3.4 \mu\text{m}^{-2} \text{min}^{-1}$), and an increase in track stalling (19 ± 9 % versus 0.7 ± 0.3 %) (Fig. 2F-H, Fig. S3H). After 10 min of culturing, the CLTA-TagRFP-T^{EN} and DNM2-eGFP^{EN} lifetimes began to recover, most likely reflecting cellular adaptation to the hypotonic treatment (Fig. 2C-H, Supp. movie 3). We did not detect effects of hypotonic media treatment on lifetimes of tracks containing only CLTA-TagRFP-T^{EN}, characteristic of structures not associated with CME (Fig. S3A,C,E,G) (36). DNM2-eGFP^{EN}-only events showed a moderate response to elevated membrane tension. We conclude that elevating plasma membrane tension with hypotonic shock markedly perturbs CME dynamics in a dose-dependent manner.

Actin force generation assists early clathrin coat deformation under elevated membrane tension

Next we determined the stage of CME at which branched actin filament assembly becomes important under elevated membrane tension. Branched actin networks are generated by activated Arp2/3 complex (37). We inhibited Arp2/3 complex-mediated actin polymerization using the small molecule CK666 (38, 39). Since Arp2/3 complex inhibition can affect membrane tension (40), we first carefully established experimental conditions in which effects of high membrane tension or CK666 would not mask one another. Treatment of cells with 100 μM CK666 did not affect the membrane tether force in these cells ($p > 0.5$) during the time the experiment was performed (Fig. S4A). Under these optimized conditions, we performed live-cell fluorescence

microscopy and STORM to learn more about the CME stages at which branched actin network assembly is required.

We first titrated CK666 and monitored the effect on CME dynamics after 4 min of treatment. We aimed to identify a minimal CK666 concentration that induced a rapid effect on CME dynamics. 100 μ M CK666 extended lifetimes of CLTA-TagRFP-T^{EN} to 79 ± 66 s after 2 mins of treatment compared to 56 ± 40 s for the DMSO control (Figs. 3B, S4B, Table S2). Similarly, DNM2-EGFP^{EN} lifetimes increased to 65 ± 64 s upon CK666 treatment, compared to 49 ± 38 s for the DMSO control (Figs. 3C and S4B). 100 μ M CK666 did not affect CME completion frequency or the percentage of persistent CLTA-TagRFP-T^{EN} tracks (Fig. S4 C and D), though we observed a small decrease in the CME initiation rate (Fig. S4E).

The elongation of DNM2-eGFP^{EN} and CLTA-TagRFP-T^{EN} lifetimes upon 100 μ M CK666 treatment was exacerbated upon simultaneous CK666 treatment in combination with moderately hypotonic (150 mOsm) media. Compared to controls, the combination of 100 μ M CK666 and 150 mOsm hypotonic media markedly lengthened the clathrin lifetimes to 96 ± 86 s (compared to DMSO control 59 ± 52 s) and dynamin2 to 84 ± 85 s (compared to DMSO control 47 ± 49 s) (Fig. 3D-F, Table S3). We conclude that in these cells, Arp2/3 complex-mediated actin assembly is required to maintain normal CME dynamics under elevated membrane tension.

Next, we used STORM to identify the precise CME stages during which Arp2/3-nucleated branched actin network force contributes to endocytic progression when membrane tension is elevated. We used STORM to determine whether specific CME stages were enriched upon drug and osmolarity treatment. Cells were cultured under the CK666 and osmolarity conditions described above, chemically fixed, and then immunolabeled for clathrin. Clathrin coat height served as a metric for the membrane invagination stage. As in the above 2d-3D STORM

experiments, the full progression from a flat clathrin coat to a rounded vesicle could be clearly resolved in 3D (Fig. 3G, lower image panel). Control cells treated with DMSO showed an average clathrin coat height of 98 ± 21 nm (Fig. 3H, Fig. S4 F). The average height increased to 106 ± 27 nm when cells were treated with $100\mu\text{M}$ CK666 (Fig. 3J). Thus, when Arp2/3 complex activity is inhibited in these cells, more clathrin pits accumulate at a greater height. This suggests that more clathrin pits stall at a later stage of progression, corresponding to the transition from the U to Ω shape (Boulant et al. 2011).

Interestingly, when Arp2/3-mediated actin polymerization was inhibited in cells with elevated membrane tension, the average clathrin coat height decreased to $96 \text{ nm} \pm 24 \text{ nm}$ (Fig. 3G and H, Fig. S4F). This height decrease was also reflected in an accumulation of smaller shape indices and a very mild effect on clathrin coat width (Fig. S4 F – H). This result suggests that, under hypotonic media conditions presumably elevating membrane tension, inhibiting Arp2/3 complex activity may slow the transition from a shallow invaginated coat to a U-shaped coat.

These data support the conclusion that under isotonic conditions, Arp2/3 complex-mediated actin force generation facilitates the U-shaped to Ω -shaped clathrin coat transition. When membrane tension is increased, Arp2/3 complex activity becomes critical for an earlier shape change, the transition from a shallow invagination to a U-shaped coat.

Actin organization adapts to elevated membrane tension by increasing clathrin coat coverage

Finally, we used STORM to determine the relationship between elevated membrane tension and actin cytoskeleton organization at CME sites (Fig. 4). We treated cells with strong (75 mOsm) hypotonic shock for 5 min and then chemically fixed them for 2c-3D STORM. When we super-resolved clathrin and actin by 2c-3D STORM in these cells, the actin cytoskeleton remained intact (41) and associated with CCSs (Fig. S5 A - D).

Strikingly, in response to hypotonic media treatment, the average actin height dramatically increased at all endocytic stages (Fig. 4B and S5 E-G). Overall the average actin height increased from 130 ± 30 nm under isotonic media conditions to 160 ± 40 nm (Fig. 4C). This increase corresponded to an increase of actin growth over the clathrin coat from covering $66 \pm 23\%$ of the coat to covering $73 \pm 21\%$ under 75 mOsm hypotonic media (Fig. 4D). The height of actin was greater for all coat shapes (e.g., flat or curved pits) (Fig. 4E). Similarly, for different extents of clathrin coverage by actin, the average actin height was greater in hypotonic conditions across different levels of coat coverage (Fig. 4F). However, the extent of asymmetry between actin and clathrin signals did not significantly change compared to the isotonic condition (Fig. S5G). These observations of greater average actin height and coverage over the clathrin coat suggest that the force contribution of actin at CME sites is increased when membrane tension is elevated.

Overall, these observations lead us to conclude that under elevated plasma membrane tension, actin grows higher in the z-dimension around clathrin coats (Fig. 4G). Such an adaptive mechanism for actin organization presumably generates the required forces to ensure the efficient progression of mammalian CME under varying levels of membrane tension.

Discussion

By combining two-color, three-dimensional STORM imaging, quantitative live-cell TIRF microscopy, and AFM tether-pulling membrane tension measurements, we showed that actin assembly adapts to membrane tension changes at individual CME sites. This mechanism likely generates forces necessary for robust endocytic progression over a range of membrane tension regimes. While STORM of individual CCSs cannot attain the resolution of EM, our approach had several advantages that allowed us to gain new mechanistic insights: (1) it allowed us to sample

much larger numbers of CME sites with a preserved actin network than is possible by EM, thus permitting rigorous quantitative analysis, (2) we imaged CME sites in intact cells that had not been subjected to unroofing or extraction protocols, and (3) we were able to use antibodies and fluorescent phalloidin to unambiguously identify specific proteins at CME sites.

Actin assembly and organization adapt to elevated membrane tension

Elevating membrane tension can have a dramatic impact on CME progression in mammalian cells (5, 42–46). However, how cells adapt to compensate for increased membrane tension has not been elucidated. Our results provide critical mechanistic insights into how the CME machinery adapts to elevated membrane tension to maintain robust CME progression. We showed quantitatively that actin assembly and organization adapt to changes in membrane tension, which was measured by AFM membrane tether pulling (Fig. 2). Changes in membrane tension can in principle occur globally (entire cells) or locally (in different regions of one cell, or even within different regions of a single endocytic site) (47, 48). Since we detect different actin organizations at individual CME sites at similar stages within a single cell, these differences might reflect subcellular, local membrane tension variation.

Measurement of membrane tension changes using atomic force microscopy

Using atomic force microscopy, we measured the membrane tether force for SK-MEL-2 cells in isotonic and hypotonic conditions (Fig. 2). In isotonic conditions, the tether force was 33 ± 7 pN (Fig. 2B). This tether force is within an intermediate range measured for other cell types such as NIH3T3 cells and macrophages (49). Assuming a $100 \text{ pN}\cdot\text{nm}$ bending rigidity of the plasma membrane, this value corresponds to a membrane tension of 0.14 ± 0.04 pN/nm (50). In hypotonic conditions, the membrane tether force increased to 48 ± 17 pN, which corresponds to a doubling of membrane tension to 0.29 ± 0.04 pN/nm. Higher membrane tether values have been

reported for other cell types (49). Below we describe the process of CME under three different plasma membrane tension regimes.

Low membrane tension regime

When membrane tension is low, clathrin coat assembly provides sufficient energy to bend the underlying plasma membrane into a full spherical shape (Fig. 3) (51). We indeed found in our STORM data that 26% of clathrin coats lack actin in early, intermediate and late CME stages. This observation is consistent with mathematical modeling, which indicates that the coat can provide sufficient energy to bend the plasma membrane when membrane tension is low (0.002 pN/nm) (52). Here, we consider low membrane tension to be a value lower than those we measured for SK-MEL-2 cells (Fig. 2). Given that actin polymerization appears to be dispensable for CME in other cell types, though it still might make CME more efficient, we hypothesize that the basal membrane tension may be lower in those cell types. However, we caution the interpretation of experiments with harsher actin drug treatments, as prolonged actin inhibitor treatment of cells can perturb the actin cortex and reduce the tether force measurements (membrane tension) by a factor of ~50% (11). Interestingly, in our STORM images, the CME sites that did not have detectable actin generally showed a very low actin cortex density (Fig. S6 A and B). The lack of an actin cortex in those regions might reflect lower membrane tension and therefore lack of a need for actin assembly in this tension regime. In future studies, strategies should be developed to relate local membrane tension to specific endocytic site geometry and actin organization.

Intermediate tension regime

In the intermediate tension regime, defined as the resting tension of SK-MEL-2 cells in isotonic conditions (Fig. 2), clathrin coat assembly and membrane curvature-inducing proteins still appear to provide sufficient energy to drive clathrin coats from the shallow to U shape (Fig. 4,

intermediate membrane tension). When we inhibited Arp2/3-mediated actin polymerization using CK666, clathrin coat progression stalled at an aspect ratio corresponding to the U-shaped stage, consistent with the effects of actin assembly inhibition reported for other cell types (5, 13, 14). Thus, at intermediate membrane tension it appears that actin force generation is primarily required for the U-shaped to Ω -shaped clathrin coat transition. The concentration of the actin network near the base of the pit may reflect a role driving plasma membrane neck constriction and scission by generating forces orthogonal to the direction of membrane invagination.

High membrane tension regime

Our live-cell and STORM observations indicate that as membrane tension is elevated further, deformation and membrane invagination during the early stages of CME become increasingly dependent upon actin force generation (Fig. 4). When membrane tension was elevated to an intermediate level (e.g. 150 mOsm media), CME lifetimes slowed modestly (Fig. S3). When we inhibited Arp2/3-mediated actin polymerization using CK666 in cells treated with 150 mOsm media, the clathrin coat was flatter than in CK666-treated cells cultured under isotonic conditions, likely reflecting an enrichment of shallow pits (Fig. 3H). Actin assembly from the base of the CCP continues until the network covers the clathrin coat completely, allowing it to interact with proteins linking the actin network to the clathrin coat (19–21). Actin-binding linker proteins such as Hip1R and Epsin1 cover the clathrin coat completely and are thus positioned to provide high internalization efficiency by harnessing actin assembly forces perpendicular to the plasma membrane (17).

An important question concerns the nature of the adaptive mechanism that increases actin assembly in response to elevated membrane tension. Possible mechanisms include: (1) stalling allows actin to assemble longer; or (2) tension increases contact of filaments in the coated pit-

associated actin network with membrane-associated N-WASP-Arp2/3 complex, leading to more assembly (17).

When the actin network fully covers the clathrin coat, it resembles the radial organization described by mathematical modeling for mammalian CME and the actin network organization described for budding yeast (17, 27, 52, 53). In yeast this actin organization drives endocytic membrane invagination against the high resistance resulting from turgor pressure. Mathematical modeling showed that this organization produces high forces perpendicular to the plasma membrane (52). Actin-generated forces parallel and orthogonal to the membrane invagination at high tension may coexist to drive membrane invagination followed by scission.

CME dynamics dramatically slow down when cells are in this high membrane tension regime, resulting in only ~40% of endocytic lifetimes shorter than 50 s and ~19% longer than the 4.8 min movies we captured, a 20-fold increase (Fig. 2). We suggest that this tension regime pushes this adaptive mechanism to the limit.

N-WASP spatial organization suggests an actin force generation control mechanism

N-WASP spatial organization at CCSs and CCPs provides valuable mechanistic insight into how actin network assembly contributes to force generation during CME. We found that N-WASP localized at the base of early and late clathrin-coated pits, where it likely interacts with SH3 domain-containing proteins present at the endocytic membrane neck (14, 21, 54). This organization is similar to that of the homologous nucleation promoting factor Las17 in budding yeast (27). Filaments nucleated at the base of CCPs would be able to interact with coat proteins such as Hip1R and Epsin1/2/3 to generate forces to invaginate the plasma membrane (17, 27, 52).

Intriguingly, we also sometimes observed a strikingly different N-WASP spatial organization in which it was distributed over the full clathrin coat. The type II nucleation factors

Abp1 and cortactin bind to actin filaments and to the Arp2/3 complex and could serve as binding partners for N-WASP around the clathrin-coated pit (55–58) (Le Clainche et al. 2007; Pinyol et al. 2007; Helgeson and Nolen 2013; Guo et al. 2018). This WASP location might reflect a distinct mechanism of filament assembly from the coat that is potentially important to generate higher forces when actin already surrounds the clathrin-coated pit.

A burst of actin assembly was shown previously to often accompany CME (59) and to facilitate CME progression, especially when membrane tension is high (5, 60). In this study we observed that CME-associated actin assembly and ultrastructural organization buffer changes in plasma membrane tension, thereby ensuring the progression of a flat clathrin coat to a round clathrin-coated vesicle over a range of membrane tension regimes. We expect that the capability of actin to buffer changes in membrane tension is a common critical feature in membrane remodeling events.

Materials and Methods:

Cell culture: SK-MEL-2 cells from clone Ti13 (hCLTA^{EN-1} /hDNM2^{EN-1}) were cultured in DMEM/F12 with GlutaMax™ supplement (10565-018, Thermo Fisher Scientific) media containing 10% fetal bovine serum (FBS) and 1,000 U/mL penicillin-streptomycin mix (15140122, Thermo Fisher Scientific) and kept in a 37°C humidified incubator with 5% CO₂ (cell source information in (31)). After each cell vial was thawed, cells were checked after 2 passages for mycoplasma contamination. Cell line authentication was performed by short tandem repeat validation.

Antibodies and reagents: The primary antibodies used were mouse anti-clathrin light chain (AB CON.1, MA5-11860, Thermo Fisher Scientific), mouse anti-clathrin heavy chain (AB X-22, MA1-065, Thermo Fisher Scientific) and rabbit anti-N-WASP (ab126626, Abcam). The secondary antibodies used were Alexa Fluorophore 647 chicken anti-rabbit (A21443, Thermo Fischer Scientific), goat anti-mouse (115-005-205, Jackson ImmunoResearch) conjugated to CF680-NHS ester (Biotium 92139). Reagents and small molecule inhibitors used were DMSO (D2650, Sigma Aldrich), CK666 (SML0006, batch # 0000012761, Sigma Aldrich) and Phalloidin-AF647 (A22287, Fisher Scientific).

Preparation of CF680-labeled secondary goat anti-mouse antibody: CF680 NHS ester was dissolved at a concentration of 3 mM in anhydrous DMSO. 1 μL of dye solution, 80 μL of a 1.25 mg/mL suspension of unlabeled goat anti-mouse IgG1 secondary antibody (115-005-205, Jackson ImmunoResearch Laboratories, Inc.), and 10 μL of 1M sodium bicarbonate solution were mixed and allowed to react for 15 min at room temperature. The reaction mixture was added to an equilibrated NAP-5 column (Sigma GE17-0853-01) and flushed with PBS. The dye conjugated antibody was collected from the first colored eluent fraction and a concentration of 0.12mg/mL was determined with a NanoDrop spectrophotometer.

Sample preparation for two-color clathrin and actin imaging: 18 mm round coverslips were cleaned 20 min in 70% ethanol (Electron Microscopy Science, Cat # 72222-01). Cells were detached with 500uL 0.05% trypsin (25300-054, Gibco), washed once in DMEM/F12 and

collected by centrifugation. Cells were counted using a hemocytometer and 20,000 cells/mL were seeded onto 18 mm round coverslips in 12-well plates. Cells were incubated for 16 – 24 hours in culture media prior to preparation for imaging.

Cells were fixed first for 1-2 min in 0.3% (v/v) glutaraldehyde (GA) solution containing 0.25% (v/v) Triton in cytoskeleton buffer (CB: 10mM MES, 150mM NaCl, 5mM EGTA, 5mM Glucose, 5mM MgCl₂, 0.005% NaN₃, pH6.1) and then immediately fixed for 10 min in 2% (v/v) GA solution in CB. Both solutions were prepared fresh from a 70% GA stock (Electron Microscopy Science, cat #16365) (protocol follows reference: (28)). After fixation, samples were washed once in CB and then incubated for 7 min in freshly prepared CB containing 0.1% (w/v) NaBH₄. Subsequently, samples were washed 3 times for 10 min in CB with gentle agitation on a shaker. Samples were then blocked for 30 min in 5% (w/v) BSA in CB (Sigma Aldrich, A3733). For dense clathrin labeling, light (diluted 1:200) and heavy chain (diluted 1:200) antibodies were used together in a 1% (w/v) BSA CB solution. Primary antibody immunostaining was performed overnight at 4°C. On the next day, samples were washed twice in 1% (w/v) BSA CB for 5 min. The mouse secondary antibody-CF680 was used at a final concentration of 0.40 µg/mL – 0.60 µg/mL in a 1% BSA - 1x CB solution. Samples were stained for 30 min at room temperature in the dark and washed twice for 5 min in 1% (w/v) BSA CB solution, and then for 10 min in CB solution. Samples were then placed into a solution of CB containing 0.5µM Phalloidin-AF647 and kept at room temperature in the dark for a minimum of 2 hours. Samples were washed once with PBS before STORM imaging.

Sample preparation for single-color clathrin and dual-color N-WASP imaging: Cells were prepared as for the two-color sample preparation on coverslips, and then fixed for 20 minutes in 3% (v/v) paraformaldehyde (PFA, 15710 Electron Microscopy Sciences) in CB (protocol follows (61)). Samples were washed quickly in CB and subsequently were incubated for 7 min in freshly prepared 0.1% (w/v) NaBH₄ in CB solution. Subsequently, samples were washed 3 times for 10 min in CB with gentle agitation on a shaker and permeabilized afterwards in a 0.1% Triton-PBS solution for 1-2 min. For single antibody clathrin staining, subsequent washing, blocking and antibody incubation steps were similar to the two-color clathrin and actin sample preparation protocol.

Dual-color immunolabeling was performed with primary antibody against N-WASP (diluted 1:200), clathrin heavy and clathrin light chain (diluted 1:600 -1:1000) in 1% (w/v) BSA in PBS overnight at 4°C. Samples were washed the next day twice for 5 min in 1% (w/v) BSA in PBS. Secondary antibody staining was first performed with Alexa Fluorophore 647 anti-rabbit antibody (diluted 1:200) in 1% BSA (w/v) in PBS for 30 min at room temperature and kept in the dark. After two 10 min long washes in PBS containing 1% (w/v) BSA, secondary antibody staining was performed with CF680 anti-mouse antibody (diluted 1:600). The samples were given three final washes in PBS for 10 min each.

SRM imaging: Dye-labeled cell samples were mounted on glass slides in a standard STORM imaging buffer consisting of 5% (w/v) glucose, 100 mM cysteamine, 0.8 mg/mL glucose oxidase, and 40 µg/mL catalase in 1M Tris-HCL (pH 7.5) (62, 63). Coverslips were sealed using Cytoseal 60. STORM imaging was performed on a homebuilt setup (64) based on a modified Nikon Eclipse Ti-U inverted fluorescence microscope using a Nikon CFI Plan Apo λ 100x oil immersion objective (NA 1.45). Dye molecules were photoswitched to the dark state and imaged using a 647-nm laser (MPB Communications); this laser was passed through an acousto-optic tunable filter and introduced through an optical fiber into the back focal plane of the microscope and onto the sample at an intensity of ~2 kW cm⁻². A translation stage was used to shift the laser beam toward the edge of the objective so the light reached the sample at incident angles slightly smaller than the critical angle of the glass-water interface. A 405-nm laser was used concurrently with the 647-nm laser to reactivate fluorophores into the emitting state. The power of the 405-nm laser (typical range 0-1 W cm⁻²) was adjusted during image acquisition so that at any given instant, only a small, optically resolvable fraction of the fluorophores in the sample was in the emitting state. For 3D STORM imaging, a cylindrical lens was inserted into the imaging path so that images of single molecules were elongated in opposite directions for molecules on the proximal and distal sides of the focal plane (62). The raw STORM data were analyzed according to previously described methods (62, 63). Data were collected at a frame rate of 110 Hz for a total of ~80,000 frames per image. Single and two-color imaging was performed on cells labeled with Alexa Fluor 647 only or Alexa Fluor 647 and CF680 with 647-nm excitation based on a ratiometric detection scheme (65–67). In the two-color imaging scheme, light emitted from the AF647 and CF680 fluorophores was collected concurrently and split into two light paths using a long pass dichroic

mirror (T685lpxr; Chroma). Each light path was projected onto one half of an Andor iXon Ultra 897 EM-CCD camera. Dye assignment was performed by localizing and recording the intensity of each single molecule in each channel. Conventional imaging of 560- and 488-nm dyes was performed immediately prior to STORM imaging using the appropriate laser and filter set. Emission data were collected through the short wavelength reflected path of the aforementioned optical setup and overlaid directly onto the final STORM image.

Selection of clathrin-coated super-resolved structures for image analysis: Clathrin-containing structures were extracted from processed STORM images using a custom MATLAB routine. Briefly, a kernel convolution with a disk of ~80 nm radius was performed on the super-resolved clathrin image channel to accentuate possible clathrin-coated pits. The resulting image was median filtered, and peaks were detected by sequentially identifying and cropping out regions corresponding to the local image maxima. 310 nm x 310 nm wide square regions centered at these peaks were cropped from all color channels and aligned. Subsequently, we selected super-resolved clathrin coats by visual inspection for further quantitative image analysis based on the following criteria: We excluded clathrin labeled structures for image analysis that appeared deformed, that covered nearly the entire 310 nm x 310 nm wide square, or that contained small punctuated structures which were not distinguishable from background noise or small clathrin seeds (Fig. S1 A). Clathrin-coated structures selected for analysis were first inspected to determine whether they appeared round-shaped, elliptical-shaped or triangle-shaped in the x-y projected super-resolved image. These images were 3D rendered to determine whether the x-z projection resulted in the typical wide-crescent shape, U-shape or round-shape appearance for the clathrin coat. If we could identify the stereotypical clathrin-coat shapes in both projections, we included the clathrin-coat in the pool for further image analysis. We define stereotypical shapes of individual clathrin coats based on platinum replica EM data of clathrin-coated pits in the same cell type (Fig. S7) (courtesy of Justin Taraska). We then assigned the clathrin coats as being actin-negative when the number of localizations in the actin channel in the 310 nm x 310 nm ROI was below 50, which is close to the background level (Fig. S6 A and B). Clathrin-coated structures were classified as actin-positive when the number of localizations in the actin channel in the 310 nm x 310 nm ROI were above 50 and actin signal overlapped with the clathrin signal.

STORM image data display in figures: Reconstructed super-resolution images were visualized using the “insight” software package and saved in a .png file format (62). These images were loaded into ImageJ, converted from an RGB image into an 8 bit image, pseudocolored for clathrin = red hot lookup table, actin = cyan lookup table, and then converted back into an RGB image.

Image analysis of reconstructed clathrin and actin side views: Selected reconstructed super-resolved images of clathrin and actin were treated as digital images for further analysis. A custom-written Jupyter notebook script was used to project reconstructed side views of clathrin and actin onto their x- and z-axis to obtain histograms of the clathrin and actin pixel intensity signals normalized to their respective maximum intensity value (Fig. S1 B and C). From these normalized z-axis and x-axis pixel intensity histograms we read out the height and width of clathrin and actin at the 30th percentile. This process resulted in more robust results than the read out at the full width at half maximum (Fig. S1 B and C).

Actin and clathrin coat height: The z-axis intensity histograms were used to report the actin and clathrin coat heights in the x-z projections. Before extracting the values, a mean filter (50) was run over the histograms to reduce signal fluctuations that interfere with the size measurement (Fig. S1 B and C).

Actin-clathrin overlap calculation: We calculated the total overlap between clathrin and actin using the indices obtained at the upper position of clathrin and lower position of actin at the 30th percentile of the respective z - axis projected intensity histograms (Fig. S1 B). We then reported the overlap relative to the clathrin height in units of percentage.

Clathrin-coat width: We used the 30th percentile of x-axis intensity histogram to report the clathrin coat width in the x-z projection. Before extracting the values, a median filter (100) was run over the histogram to smooth out signal fluctuations that interfere with the correct size determination (Fig. S1 B and C).

Shape index calculation: Shape indices of individual clathrin structures are defined as the ratio between clathrin coat height and clathrin coat width. This value allowed us to sort flat (low shape index) and rounded (high shape index) clathrin coats from each other.

Asymmetry of actin signal around clathrin coat: To evaluate the asymmetry of the spatial actin organization around the clathrin coat, we determined the difference in the positions of the peak

actin and clathrin signals on both x-z and y-z projections of our images (Fig. S1 E). We obtained the center of the clathrin coat in nm by rendering the clathrin super-resolved image into a diffraction limited image, as explained in paragraph ‘Selection of clathrin-coated super-resolved structures for image analysis’. We first identified the position of the actin maximum intensity in the x-z projection profile and y-z projection profile in nm. Then we measured the distance of these obtained position to the middle position of the clathrin intensity profile. This distance measurement is proportional to the asymmetry of the actin position with respect to clathrin; namely a low distance corresponds to high symmetry and a high distance corresponds to high asymmetry in the position of the actin signal.

Total internal reflection fluorescence (TIRF) microscopy: TIRF imaging was carried out on a Nikon Eclipse Ti2 inverted microscope with a CFI60 60x Apo TIRF objective and a Hamamatsu Orca-Flash 4.0 V2 sCMOS camera. eGFP and Tag.RFP-T fluorescence were excited using 488 nm and 561 nm lasers and detected using a Chroma HC TIRF Quad Dichroic (C-FL TIRF Ultra Hi S/N 405/488/561/638) and Chroma HC Quad emission filters BP 525/50 and BP600/50, respectively (Bellows Falls, VT). Unless mentioned specifically, channels were acquired sequentially at a 1.2 sec interval and 400ms exposure time over 4.8 minutes to 6 minutes. Real-time acquisition was achieved by a National Instruments (PXI 1033, Austin, TX) controller. The system was controlled with NIS-Elements software and maintained at 37°C by an OkoLab environmental chamber (Burlingame, CA).

Hypo-osmotic media treatment: SK-MEL-2 cells were plated on glass coverslips one day prior to osmotic treatment and imaging: 20,000 cells/ mL were seeded 16h – 24h prior to the experiment on 25 mm round #1.5 glass coverslips that had been cleaned with 70% ethanol (Warner Instruments, 64-0715). Isotonic imaging media contained Dulbecco’s Modified Essential Medium and Ham’s F-12 medium (DMEM/F12) without phenol red (11039, Thermo Fisher Scientific) with 5% v/v FBS. The media was diluted with an inorganic salt solution containing 10mM CaCl₂, 0.3mM MgCl₂ and 0.1mM MgSO₄ (CMM) to maintain concentrations of critical ions, while obtaining hypo-osmotic conditions by diluting the media containing components such as D-Glucose. 225 mOsm hypotonic imaging media contained 1:4 v/v CMM solution in DMEM/F12, 150 mOsm hypotonic imaging media contained 1:1 v/v CMM solution in

DMEM/F12, and 75 mOsm hypotonic imaging media contained 4:1 v/v CMM solution in DMEM/F12. 5% v/v FBS was present in all hypotonic solutions.

For live cell fluorescence microscopy, CLTA-TagRFP-T^{EN} and DNM2-eGFP^{EN} fluorescence in SK-MEL-2 cells were acquired first in isotonic media over a course of 4.8 minutes. Subsequently, media was exchanged on the stage to hypotonic media (either 225 mOsm, 150 mOsm or 75 mOsm) and movies were acquired for 4.8 minutes, starting 2 minutes and 10 minutes after media exchange. Media exchange on the stage did not affect CME initiation rates or fluorescence lifetimes beyond the existing experimental intrinsic variability (Fig. S4 B).

For STORM imaging, 75 mOsm hypotonic buffer treatment was performed in the cell culture dish for 5 min. Cells were immediately chemically fixed after the 5 min treatment and further treated with the STORM sample preparation protocol as described above.

CK666 concentration titration: 20,000 SK-MEL-2 cells/ mL were seeded in 8 well chambers 16h – 24h prior to the experiment (80826, ibidi, Fitchburg, WC). A CK666 (SML0006, batch # 0000012761, Sigma Aldrich) stock solution was prepared at 50mM in DMSO and kept at -20°C. 25µM, 50µM and 100 µM CK666 and equivalent 0.5% v/v DMSO, 1% v/v DMSO and 2% DMSO v/v solutions for controls were prepared fresh in DMEM/F12 containing 5% FBS and kept at 37°C until used. Cells were first imaged in DMEM/F12 containing 5% FBS solution as a baseline control for 4.8 minutes. Subsequently, imaging solution was exchanged on the microscopy stage to CK666 or DMSO containing imaging solution and another 4.8-minute movie was acquired after 2 minutes of treatment. Each treatment was repeated twice and an area of 1024 pixel x 1024 pixel was used to record 3-6 cells per experiment.

CK666 in combination with hypo-osmotic media: Cells were prepared as for the CK666 concentration titration experiment described above. Solutions of 2% v/v DMSO in DMEM/F12, 100 µM CK666 in DMEM/F12, 2% v/v DMSO in 1:1 v/v CMM solution in DMEM/F12 (150 mOsm hypotonic media) and 100 µM CK666 1:1 v/v CMM solution in DMEM/F12 (150 mOsm hypotonic media) were prepared fresh and kept at 37°C until used. All solutions contained 5% FBS. Cells were first imaged in DMEM/F12-5% FBS solution as a baseline control for 6 minutes. Subsequently, the imaging solution was exchanged on the microscopy stage to the desired experimental solutions and a 6-minute movie was recorded after 4 minutes of incubation.

Image analysis of TIRF live-cell microscopy data: Fluorescent diffraction-limited spots of DNM2-eGFP^{EN} and CLTA-TagRFP-T^{EN} in SK-MEL-2 cells were tracked in each channel over the course of the movie using the detection and tracking features of the cmeAnalysis software package in Matlab (68). Subsequently, we cleaned up the background signal and, based on the x and y positions of associated CLTA-TagRFP-T^{EN} and DNM2-eGFP^{EN} fluorescent tracks, separated them from CLTA-TagRFP-T^{EN} and DNM2-eGFP^{EN} that were not associated with each other, using a custom-written Matlab script (10, 36, 42). We measured fluorescence lifetimes for DNM2-eGFP^{EN} and CLTA-TagRFP-T^{EN} tracks that were associated and not associated with each other and that appeared and disappeared within the duration of a movie. We classified the tracks as “persistent” when they were already present in the first movie frame and lasted longer than the movie.

CME initiation rate and completion rate measurement: We defined a track as initiated if it appeared within the course of the acquisition, excluding in the first frame. We classified a track as complete when it appeared and disappeared within the course of the acquisition. To calculate rates of initiation and completion, we used these values along with measurement of the area of the tracked region, which was obtained from the binary cell mask image generated during the detection step of the cmeanalysis program that highlights the cell area in which particle tracking was performed. ImageJ was then used to calculate the area of the cell from the binary mask image. The final metric is defined as the number of initiations (or completions) per area per time. In the figure we multiplied this value by 100.

Tether pulling experiments using Atomic Force Microscopy: Custom-cut 35-mm glass-bottom dishes (Greiner Bio-One, #627860) were coated with fibronectin (50 ug/mL, Corning #356008) for 30 minutes and washed with DPBS shortly before use. SK-MEL-2 cells were seeded at a density of $0.15\text{-}0.20 \times 10^5$ cells/ml in DMEM/F12 GlutaMaxTM supplement media with 1% FBS and penicillin-streptomycin mix (GibcoTM, #15140-122) in a 37°C humid incubator with 5% CO₂ for 2-4 hours, and used directly for membrane tether pulling experiments. OBL-10 cantilevers (Bruker) were mounted on a CellHesion 200 AFM (Bruker) integrated into an Eclipse Ti inverted light microscope (Nikon), calibrated using thermal noise method and coated with 2.5 mg/ml

Concanavalin A (C5275, Sigma) for 1 hour at 30°C. After rinsing the cantilever with DPBS, it was positioned at any location over the cell for tether pulling using brightfield imaging. Approach velocity was set to 1 $\mu\text{m/s}$, contact force to 100–300 pN, contact time to 300 ms–10 s, and retraction speed to 10 $\mu\text{m/s}$. After a 10 μm tether was pulled, the cantilever position was held constant until the moment of tether breakage and at least 2 seconds afterwards. Sampling rate was set to 2000 Hz. After measurements of tether forces in control conditions, an inorganic salt solution containing 10mM CaCl_2 , 0.3mM MgCl_2 and 0.1mM MgSO_4 was added to the medium (4:1 v/v) to achieve 75 mOsm hypotonic treatment. Tether forces were measured after media dilution for 2-16 minutes. Tether forces per cell are the average of at least 3 tethers. Cells were not used longer than 1 h for data acquisition. Force-time curve analysis was performed using the JPKSPM Data Processing Software.

Data analysis, statistical analysis and data plotting: For statistical analysis and data plotting, Prism version 7.0e and matplotlib in a Jupyter notebook (5.5.0) were used.

Online supplemental material: Fig. S1 gives an overview of clathrin structure selection and parameter extraction of super-resolved clathrin and actin. Representative x-y STORM image projections are shown of super-resolved clathrin and actin corresponding to the images in Fig. 1, and describes the measurement of asymmetry between clathrin and actin signals. Fig. S2 shows STORM images of super-resolved clathrin and N-WASp. In Fig. S3 we present additional data from live cell imaging of SK-MEL-2 cells endogenously expressing CLTA-TagRFP-T^{EN} and DNMT2-eGFP^{EN} in hypotonic and isotonic control media. Fig S4 shows measurements of membrane tether force \pm CK666, establishes the CK666 concentration affecting CME in SK-MEL-2 cells, and provides additional data on CK666 and concomitant hypotonic media treatment. Fig. S5 provides additional data on the effect of hypotonic media treatment on actin organization. Fig. S6 shows x-y STORM projections of clathrin-coated pits unassociated with actin. Fig. S7 shows examples of single and double clathrin-coated pits based on size comparison to platinum replica electron micrographs. Table S1 reports the lifetimes of endocytic tracks in isotonic and hypotonic conditions. Table S2 reports the lifetimes of endocytic tracks in cells treated with CK666. Table S3 reports the lifetimes of endocytic tracks in cells in hypotonic conditions and treated with CK666.

References

1. M. Kaksonen, Y. Sun, D. G. Drubin, A pathway for association of receptors, adaptors, and actin during endocytic internalization. *Cell* **115**, 475–487 (2003).
2. S. Aghamohammadzadeh, K. R. Ayscough, Differential requirements for actin during yeast and mammalian endocytosis. *Nat. Cell Biol.* **11**, 1039–1042 (2009).
3. F. Z. Idrissi, A. Blasco, A. Espinal, G. M, Ultrastructural dynamics of proteins involved in endocytic budding. *National Acad Sciences* (2012).
4. W. Kukulski, M. Schorb, M. Kaksonen, J. A. G. Briggs, Plasma membrane reshaping during endocytosis is revealed by time-resolved electron tomography. *Cell* **150**, 508–520 (2012).
5. S. Boulant, C. Kural, J. C. Zeeh, F. Ubelmann, T. Kirchhausen, Actin dynamics counteract membrane tension during clathrin-mediated endocytosis. *Nat. Cell Biol.* **13**, 1124–1131 (2011).
6. S. Kaur, A. B. Fielding, G. Gassner, N. J. Carter, S. J. Royle, An unmet actin requirement explains the mitotic inhibition of clathrin-mediated endocytosis. *Elife* **3**, 1039–1017 (2014).
7. A. Grassart, *et al.*, Actin and dynamin2 dynamics and interplay during clathrin-mediated endocytosis. *J. Cell Biol.* **205**, 721–735 (2014).
8. L. M. Fujimoto, R. Roth, J. E. Heuser, S. L. Schmid, Actin assembly plays a variable, but not obligatory role in receptor-mediated endocytosis in mammalian cells. *Traffic* **1**, 161–171 (2000).
9. C. J. Merrifield, D. Perrais, D. Zenisek, Coupling between clathrin-coated-pit invagination, cortactin recruitment, and membrane scission observed in live cells. *Cell* **121**, 593–606 (2005).
10. D. Dambournet, *et al.*, Genome-edited human stem cells expressing fluorescently labeled endocytic markers allow quantitative analysis of clathrin-mediated endocytosis during differentiation. *J. Cell Biol.* **2**, jcb.201710084-11 (2018).
11. B. Pontes, P. Monzo, N. C. Gauthier, Membrane tension: A challenging but universal physical parameter in cell biology. *Semin. Cell Dev. Biol.* **71**, 30–41 (2017).
12. U. Djakbarova, Y. Madraki, E. Chan, C. Kural, Dynamic interplay between cell membrane tension and clathrin-mediated endocytosis. *Biol. Cell* (2021)
<https://doi.org/10.1111/boc.202000110>.
13. D. Yarar, C. M. Waterman-Storer, S. L. Schmid, A dynamic actin cytoskeleton functions at multiple stages of clathrin-mediated endocytosis. *Mol. Biol. Cell* **16**, 964–975 (2005).

14. L. Almeida-Souza, *et al.*, A Flat BAR Protein Promotes Actin Polymerization at the Base of Clathrin-Coated Pits. *Cell* **174**, 325-337.e14 (2018).
15. P. Bieling, *et al.*, Force Feedback Controls Motor Activity and Mechanical Properties of Self-Assembling Branched Actin Networks. *Cell* **164**, 115–127 (2016).
16. J. Mueller, *et al.*, Load Adaptation of Lamellipodial Actin Networks. *Cell* **171**, 188-200.e16 (2017).
17. M. Akamatsu, *et al.*, Principles of self-organization and load adaptation by the actin cytoskeleton during clathrin-mediated endocytosis. *Elife* **9** (2020).
18. A. Collins, A. Warrington, K. A. Taylor, T. Svitkina, Structural organization of the actin cytoskeleton at sites of clathrin-mediated endocytosis. *Curr. Biol.* **21**, 1167–1175 (2011).
19. A. E. Engqvist-Goldstein, *et al.*, The actin-binding protein Hip1R associates with clathrin during early stages of endocytosis and promotes clathrin assembly in vitro. *J. Cell Biol.* **154**, 1209–1223 (2001).
20. M. Messa, *et al.*, Epsin deficiency impairs endocytosis by stalling the actin-dependent invagination of endocytic clathrin-coated pits. *Elife* **3**, e03311 (2014).
21. K. A. Sochacki, A. M. Dickey, M.-P. Strub, J. W. Taraska, Endocytic proteins are partitioned at the edge of the clathrin lattice in mammalian cells. *Nat. Cell Biol.* **12**, 517–541 (2017).
22. N. I. Clarke, S. J. Royle, FerriTag is a new genetically-encoded inducible tag for correlative light-electron microscopy. *Nat. Commun.* **9**, 1–10 (2018).
23. S. Y. Carroll, *et al.*, Analysis of yeast endocytic site formation and maturation through a regulatory transition point. *Mol. Biol. Cell* **23**, 657–668 (2012).
24. M. Skruzny, *et al.*, Molecular basis for coupling the plasma membrane to the actin cytoskeleton during clathrin-mediated endocytosis. *Proc. Natl. Acad. Sci. U. S. A.* **109**, E2533-42 (2012).
25. M. Skruzny, *et al.*, An organized co-assembly of clathrin adaptors is essential for endocytosis. *Dev. Cell* **33**, 150–162 (2015).
26. A. Picco, M. Mund, J. Ries, F. Nédélec, M. Kaksonen, Visualizing the functional architecture of the endocytic machinery. *Elife* **4** (2015).
27. M. Mund, *et al.*, Systematic Nanoscale Analysis of Endocytosis Links Efficient Vesicle Formation to Patterned Actin Nucleation. *Cell* **174**, 884-896.e17 (2018).
28. K. Xu, H. P. Babcock, X. Zhuang, Dual-objective STORM reveals three-dimensional filament organization in the actin cytoskeleton. *Nat. Methods* **9**, 185–188 (2012).

29. K. Xu, G. Zhong, X. Zhuang, Actin, Spectrin, and Associated Proteins Form a Periodic Cytoskeletal Structure in Axons. *Science* **339**, 452–456 (2013).
30. M. Hauser, *et al.*, The spectrin-actin-based periodic cytoskeleton as a conserved nanoscale scaffold and ruler of the neural stem cell lineage. *Cell Rep.* **24**, 1512–1522 (2018).
31. J. B. Doyon, *et al.*, Rapid and efficient clathrin-mediated endocytosis revealed in genome-edited mammalian cells. *Nat. Cell Biol.* **13**, 331–337 (2011).
32. J. Mulholland, Ultrastructure of the yeast actin cytoskeleton and its association with the plasma membrane. *J. Cell Biol.* **125**, 381–391 (1994).
33. F.-Z. Idrissi, *et al.*, Distinct acto/myosin-I structures associate with endocytic profiles at the plasma membrane. *J. Cell Biol.* **180**, 1219–1232 (2008).
34. C. Buser, D. G. Drubin, Ultrastructural Imaging of Endocytic Sites in *Saccharomyces cerevisiae* by Transmission Electron Microscopy and Immunolabeling. *Microsc. Microanal.* **19**, 381–392 (2013).
35. O. Avinoam, M. Schorb, C. J. Beese, J. A. G. Briggs, M. Kaksonen, ENDOCYTOSIS. Endocytic sites mature by continuous bending and remodeling of the clathrin coat. *Science* **348**, 1369–1372 (2015).
36. S. H. Hong, C. L. Cortesio, D. G. Drubin, Machine-Learning-Based Analysis in Genome-Edited Cells Reveals the Efficiency of Clathrin-Mediated Endocytosis. *Cell Rep.* **12**, 2121–2130 (2015).
37. T. D. Pollard, Regulation of actin filament assembly by Arp2/3 complex and formins. **36**, 451–477 (2007).
38. B. J. Nolen, *et al.*, Characterization of two classes of small molecule inhibitors of Arp2/3 complex. *Nature* **460**, 1031–1034 (2009).
39. B. Hetrick, M. S. Han, L. A. Helgeson, B. J. Nolen, Small Molecules CK-666 and CK-869 Inhibit Actin-Related Protein 2/3 Complex by Blocking an Activating Conformational Change. *Chem. Biol.* **20**, 701–712 (2013).
40. A. Diz-Muñoz, *et al.*, Membrane Tension Acts Through PLD2 and mTORC2 to Limit Actin Network Assembly During Neutrophil Migration. *PLoS Biol.* **14**, e1002474-30 (2016).
41. L. Pan, *et al.*, Hypotonic stress induces fast, reversible degradation of the vimentin cytoskeleton via intracellular calcium release. *Adv. Sci. (Weinh.)* **6**, 1900865 (2019).
42. J. P. Ferguson, *et al.*, Deciphering dynamics of clathrin-mediated endocytosis in a living organism. *J. Cell Biol.* **282**, jcb.201604128-12 (2016).
43. J. P. Ferguson, *et al.*, Mechanoregulation of clathrin-mediated endocytosis. *J. Cell Sci.* **130**, 3631–3636 (2017).

44. N. M. Willy, *et al.*, Membrane mechanics govern spatiotemporal heterogeneity of endocytic clathrin coat dynamics. *Mol. Biol. Cell* **28**, 3480–3488 (2017).
45. D. Bucher, *et al.*, Clathrin-adaptor ratio and membrane tension regulate the flat-to-curved transition of the clathrin coat during endocytosis. *Nat. Commun.* **9**, 1–13 (2018).
46. D. Raucher, M. P. Sheetz, Membrane expansion increases endocytosis rate during mitosis. *J. Cell Biol.* **144**, 497–506 (1999).
47. Z. Shi, Z. T. Graber, T. Baumgart, H. A. Stone, A. E. Cohen, Cell Membranes Resist Flow. *Cell* **175**, 1769-1779.e13 (2018).
48. P. Rangamani, K. K. Mandadap, G. Oster, Protein-Induced Membrane Curvature Alters Local Membrane Tension. *Biophysj* **107**, 751–762 (2014).
49. E. Sitarska, A. Diz-Muñoz, Pay attention to membrane tension: Mechanobiology of the cell surface. *Curr. Opin. Cell Biol.* **66**, 11–18 (2020).
50. A. Diz-Muñoz, D. A. Fletcher, O. D. Weiner, Use the force: membrane tension as an organizer of cell shape and motility. *Trends Cell Biol.* **23**, 47–53 (2013).
51. M. Saleem, *et al.*, A balance between membrane elasticity and polymerization energy sets the shape of spherical clathrin coats. *Nat. Commun.* **6**, 6249 (2015).
52. J. E. Hassinger, G. Oster, D. G. Drubin, P. Rangamani, Design principles for robust vesiculation in clathrin-mediated endocytosis. *Proc. Natl. Acad. Sci. U. S. A.* **114**, E1118–E1127 (2017).
53. S. M. Ferguson, *et al.*, Coordinated actions of actin and BAR proteins upstream of dynamin at endocytic clathrin-coated pits. *Dev. Cell* **17**, 811–822 (2009).
54. J. Schöneberg, *et al.*, Lipid-mediated PX-BAR domain recruitment couples local membrane constriction to endocytic vesicle fission. *Nat. Commun.* **8**, 15873 (2017).
55. C. Le Clainche, *et al.*, A Hip1R-cortactin complex negatively regulates actin assembly associated with endocytosis. *EMBO J.* **26**, 1199–1210 (2007).
56. R. Pinyol, A. Haeckel, A. Ritter, B. Qualmann, M. M. Kessels, Regulation of N-WASP and the Arp2/3 complex by Abp1 controls neuronal morphology. *PLoS One* **2**, e400 (2007).
57. L. A. Helgeson, B. J. Nolen, Mechanism of synergistic activation of Arp2/3 complex by cortactin and N-WASP. *Elife* **2**, e00884 (2013).
58. S. Guo, *et al.*, Abp1 promotes Arp2/3 complex-dependent actin nucleation and stabilizes branch junctions by antagonizing GMF. *Nat. Commun.* **9**, 1–14 (2018).

59. C. J. Merrifield, M. E. Feldman, L. Wan, W. Almers, Imaging actin and dynamin recruitment during invagination of single clathrin-coated pits. *Nat. Cell Biol.* **4**, 691–698 (2002).
60. A. Yoshida, *et al.*, Morphological changes of plasma membrane and protein assembly during clathrin-mediated endocytosis. *PLoS Biol.* **16**, e2004786-28 (2018).
61. Y. Li, *et al.*, Real-time 3D single-molecule localization using experimental point spread functions. *Nat. Methods* **15**, 367–369 (2018).
62. B. Huang, W. Wang, M. Bates, X. Zhuang, Three-dimensional super-resolution imaging by stochastic optical reconstruction microscopy. *Science* **319**, 810–813 (2008).
63. M. J. Rust, M. Bates, X. Zhuang, Sub-diffraction-limit imaging by stochastic optical reconstruction microscopy (STORM). *Nat. Methods* **3**, 793–796 (2006).
64. M. Wojcik, M. Hauser, W. Li, S. Moon, K. Xu, Graphene-enabled electron microscopy and correlated super-resolution microscopy of wet cells. *Nat. Commun.* **6**, 1–6 (2015).
65. M. Bossi, *et al.*, Multicolor far-field fluorescence nanoscopy through isolated detection of distinct molecular species. *Nano Lett.* **8**, 2463–2468 (2008).
66. I. Testa, *et al.*, Multicolor fluorescence nanoscopy in fixed and living cells by exciting conventional fluorophores with a single wavelength. *Biophys. J.* **99**, 2686–2694 (2010).
67. A. Gorur, *et al.*, COPII-coated membranes function as transport carriers of intracellular procollagen I. *J. Cell Biol.* **216**, 1745–1759 (2017).
68. F. Aguet, C. N. Antonescu, M. Mettlen, S. L. Schmid, G. Danuser, Advances in Analysis of Low Signal-to-Noise Images Link Dynamin and AP2 to the Functions of an Endocytic Checkpoint. *Dev. Cell* **26**, 279–291 (2013).

Acknowledgments: CK was funded by the German research foundation (DFG KA4305/1-1). DGD was funded by NIH grant R35GM118149. KX was funded by NSF under CHE-1554717 and the Pew Biomedical Scholars Award. ADM was funded by the European Molecular Biology Laboratory (EMBL), the Human Frontiers Science Program (HFSP) grant number RGY0073/2018 and the Deutsche Forschungsgemeinschaft (DFG) grant numbers DI 2205/2-1 and DI 2205/3-1. MA was funded by NIH grant 1 K99 GM132551-01. ES was funded by the EMBL and the Joachim Herz Stiftung Add-on Fellowship for Interdisciplinary Science. We thank Justin Taraska and Kem Sochacki (NHLBI, NIH) for use of the platinum replica EM images for comparison in Figure S7. We thank Yidi Sun, Padmini Rangamani and Ross T.A. Pedersen for critical reading and discussions on the manuscript. We thank Sungmin Son and Daniel A. Fletcher for valuable input and discussion on the manuscript.

Abbreviations:

CME Clathrin-mediated endocytosis
CCV Clathrin coated vesicles
CCS clathrin coated structure
CCP Clathrin coated pits
SI shape index

Figure legends

Figure 1: Two-color, three-dimensional stochastic optical reconstruction microscopy (2c-3D STORM) resolves clathrin structures highly connected to actin networks at different stages of endocytosis. (A) STORM image of the ventral surface of an SK-MEL-2 cell immunolabeled with the CF-680 antibody (clathrin coats in red) and phalloidin-AF647 (actin in cyan). Orange squares are areas shown in panel B. Color bar shows the z position of actin. Scale bar: 5 μm . **(B)** Magnification of highlighted areas 1 and 2 in panel A. Magenta squares are shown in panel C. Scale bars: 250 nm. **(C)** X-Z projections of the regions highlighted in panel B. Scale bars: 100 nm. **(D)** Classification of clathrin coats (red) into geometric stages based on their aspect ratio (shape index SI). Shallow: $SI < 0.7$; U-shape: $0.7 < SI < 0.9$ and omega: $SI > 0.9$. **(E)** X-Z projections of representative STORM images showing clathrin coats (red) with different actin (cyan) coverages around clathrin. Calculated shape index of shallow CCPs from left to right image: 0.56, 0.53, 0.51, 0.55; for U-Shaped CCPs from left image to right image: 0.87, 0.89, 0.86, 0.82; for omega-shaped CCPs from left image to right image: 1.31, 1.06, 1.31, 1.52. Scale bars: 100 nm. **(F)** Graphs of endocytic coat shape index as a function of actin coverage for shallow, U-shaped and omega-shaped pits. Pits with actin coverage $>5\%$ are shown. Values in red are the percentages of clathrin coats with high ($>50\%$) actin coverage. Upper plot $R = -0.11$, $n = 150$; middle plot $R = 0.05$, $n = 220$, lower plot $R = -0.01$, $n = 347$. Events accumulated from 6 cells. **(G)** Cartoon depicting the clathrin coat with actin either at the tip of the coat (top), covering the clathrin coat completely (middle), or at the base of the clathrin coat (bottom). Dashed black lines indicate the average Z position of actin and clathrin. D_z is the difference between average actin and clathrin Z positions. $D_z < 0$ is defined as the average actin Z position nearer the base of the pit. Schematic is a hypothetical plot of D_z versus actin coverage for scenarios in which actin grows from the tip of the

coat (red line) or the base of the pit (black line). **(H)** D_z as a function of actin coverage (for actin coverage $>5\%$, $R=0.66$, $n = 719$, $N_{\text{cells}} = 6$). **(I)** Cartoon of actin (blue) growing from the base of the pit (black lines) to cover clathrin coat (red) from a shallow membrane invagination to a fully formed membrane vesicle. X-Z projection (side profile) is shown. Dashed arrows indicate that growth of the actin network is not tightly coupled to the endocytic stage and is variable in extent.

Figure 2: Quantitative analysis of clathrin-mediated endocytosis mechanosensitivity under elevated membrane tension. **(A)** Schematic of cells in isotonic media (top) or hypotonic media (bottom), which causes water influx and stretches the cell membrane. In this figure, hypotonic treatment is 75 mOsm. **(B)** Mean membrane tether force values measured by atomic-force microscopy of cells in isotonic media ($n = 18$) or in hypotonic media ($n = 17$). Mean values were obtained by pulling at least 3 tethers (3 independent experiments). In hypotonic treatment, circles are mean tether values from 2 min to 10 min after hypotonic media exchange, and triangles are mean tether values obtained between 10 min and 16 min after hypotonic media exchange. Bars are mean \pm SD. $p = 0.002$ by Mann-Whitney test. **(C)** Kymographs of total-internal reflection fluorescence micrographs of live SK-MEL-2 cells endogenously expressing CLTA-TagRFP-T^{EN} (magenta) and DNM2-eGFP^{EN} (green). Time is on the X axis. Kymographs are 4.8 min long. Cells were imaged in isotonic media (top), or hypotonic media for 2 min (middle) or 10 min (bottom). **(D)** Cumulative distribution plot of clathrin lifetimes marked by CLTA-TagRFP-T^{EN} in isotonic media (red), hypotonic media for 2 min (violet), and hypotonic media for 10 min (orange). These tracks were associated with DNM2-eGFP^{EN}. **(E)** Cumulative distribution plot of dynamin2 lifetime marked by DNM2-eGFP^{EN} in isotonic media (light green), hypotonic media for 2 min (blue), and hypotonic media for 10 min (dark green). These tracks were associated with CLTA-TagRFP-T^{EN}.

n = (5831) tracks in 17 cells across four experiments for D-H. **(D)** and **(E)** detailed statistics in Table S1. **(F)** Plot of endocytic initiation rate for the three conditions. $p < 0.05$ by Kolmogorov-Smirnov test for both comparisons. **(G)** Endocytic completion rate in the 3 conditions. $p < 0.05$ by Kolmogorov-Smirnov test for both comparisons. **(H)** Percentage of persistent tracks (defined as tracks lasting the entirety of the image acquisition) for the three conditions. **(F) - (H)** Boxplots show mean \pm SD. Statistics in Table S1 and Fig. S3H.

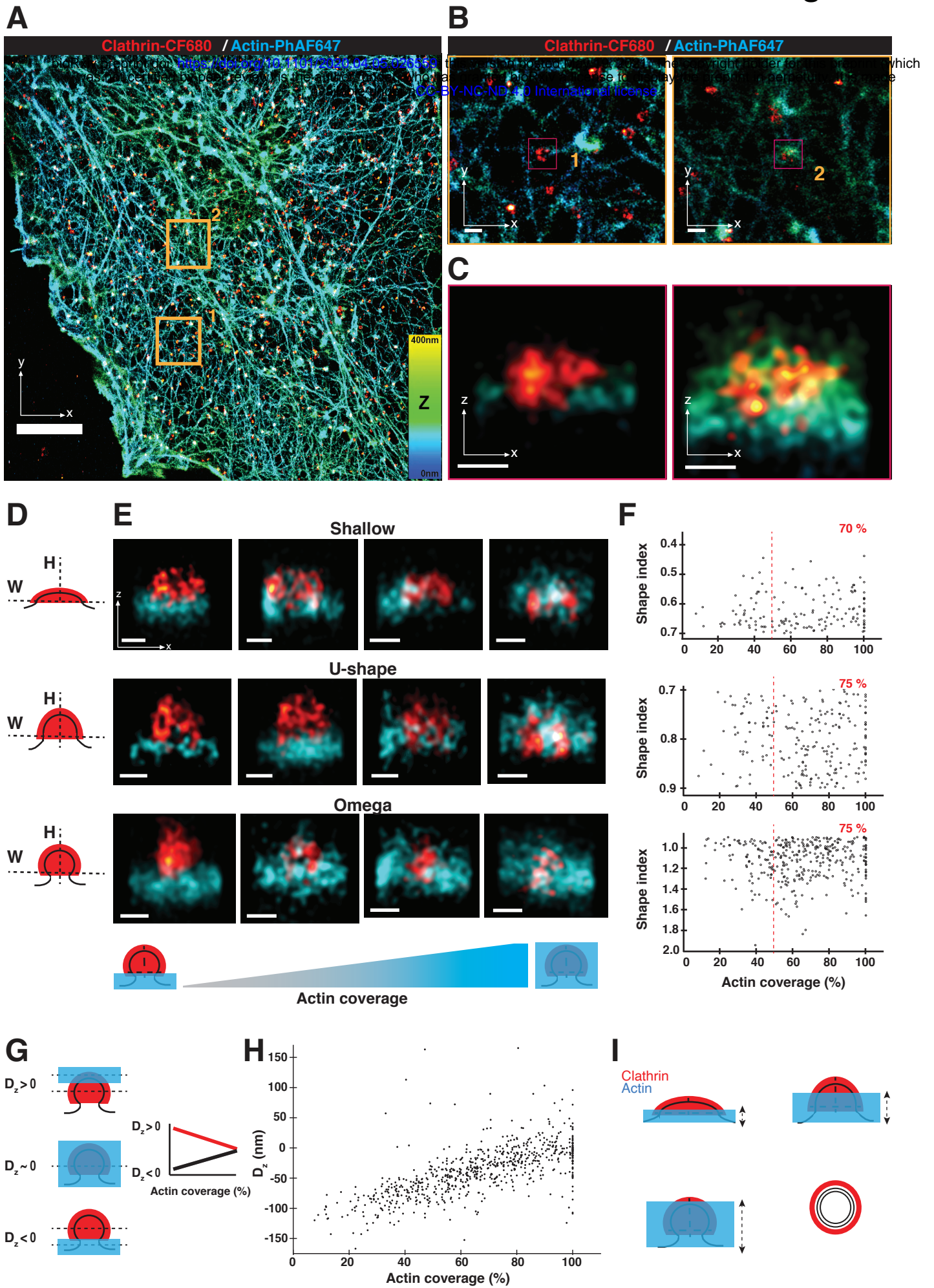
Figure 3: Importance of Arp2/3 complex-mediated actin polymerization during CME increases under elevated membrane tension. In this figure, CK666 (Arp2/3 complex inhibitor) treatment is 100 μ M and hypotonic shock is 150mOsm. **(A)** Kymographs of cells expressing CLTA-TagRFP-T^{EN} (magenta) and DNM2-eGFP^{EN} (green) imaged by total-internal reflection microscopy. Cells were imaged in isotonic media. The media was then exchanged to include CK666 (lower panel) and imaged after 4 min. **(B)** Cumulative distribution plots of clathrin lifetimes in control, DMSO-treated (orange, (n = 4219)), and CK666-treated (red, n = 3124) conditions. **(C)** Cumulative distribution plots for control, DMSO-treated (dark green, n = 4219), and CK666-treated (light green, n = 3124) dynamin2 lifetimes associated with clathrin lifetimes in (B). (B) and (C) control N_cells = 10 and CK666 treatment N_cells = 10 measured in 3 independent experiments. Complete statistics in Table S3. **(D)** Kymographs of cells in hypotonic media. In the upper panel, cells were placed in hypotonic media and imaged after 4 min. In the lower panel, cells were treated with CK666 in hypotonic media and imaged after 4 min. **(E)** Cumulative distribution plots of clathrin lifetimes for control, DMSO-treated (magenta, n = 1405), and CK666-treated (blue, n = 2783) in hypotonic media. **(F)** Cumulative distribution plots of DMSO-treated (black, n = 1405) and CK666-treated (olive, n = 2783) dynamin2 lifetimes in

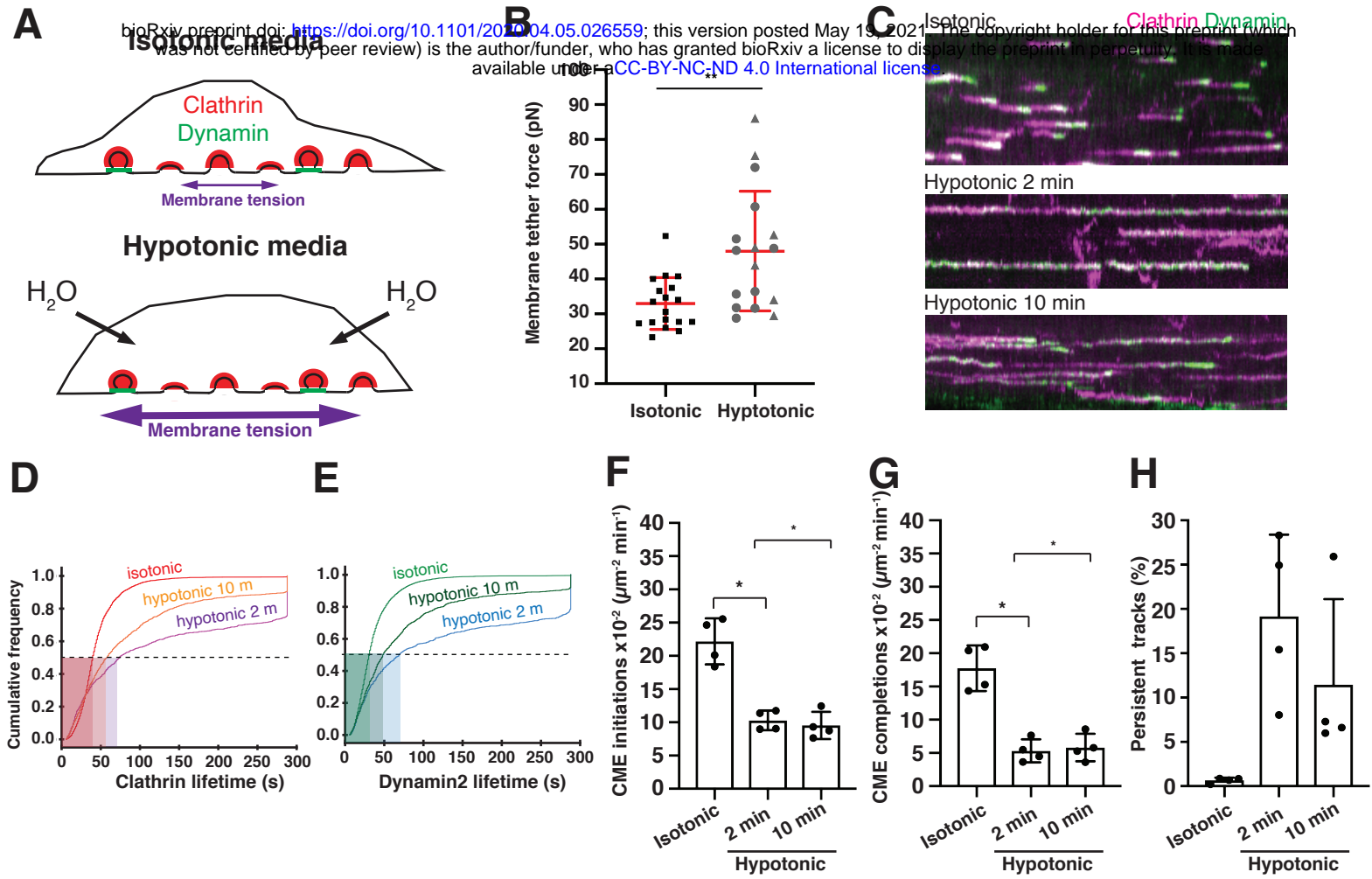
hypotonic media associated with clathrin lifetimes in (E). (E) and (F) control N_cells = 9 and CK666 treatment N_cells = 10 measured in 3 independent experiments. Complete statistics in Table S3. (G) Representative STORM images of immunolabeled clathrin-coated structures in control cells arranged by coat height. Upper panel shows the x-y projections and lower panel the corresponding x-z projections. The height of clathrin coats in the x-y projection from left to right image is 61 nm, 96 nm, 124 nm, 158 nm and 177 nm. Scale bars: 100 nm. (H) Clathrin coat heights when cells were treated with DMSO (n = 154) or CK666 (n = 158) in isotonic media or CK666 in hypotonic media (n = 159). Clathrin coat images for quantitative analysis were collected from at least 3 cells for each condition. Statistics are given in Figure S3E. $p < 0.05$ in both comparisons by Mann-Whitney test.

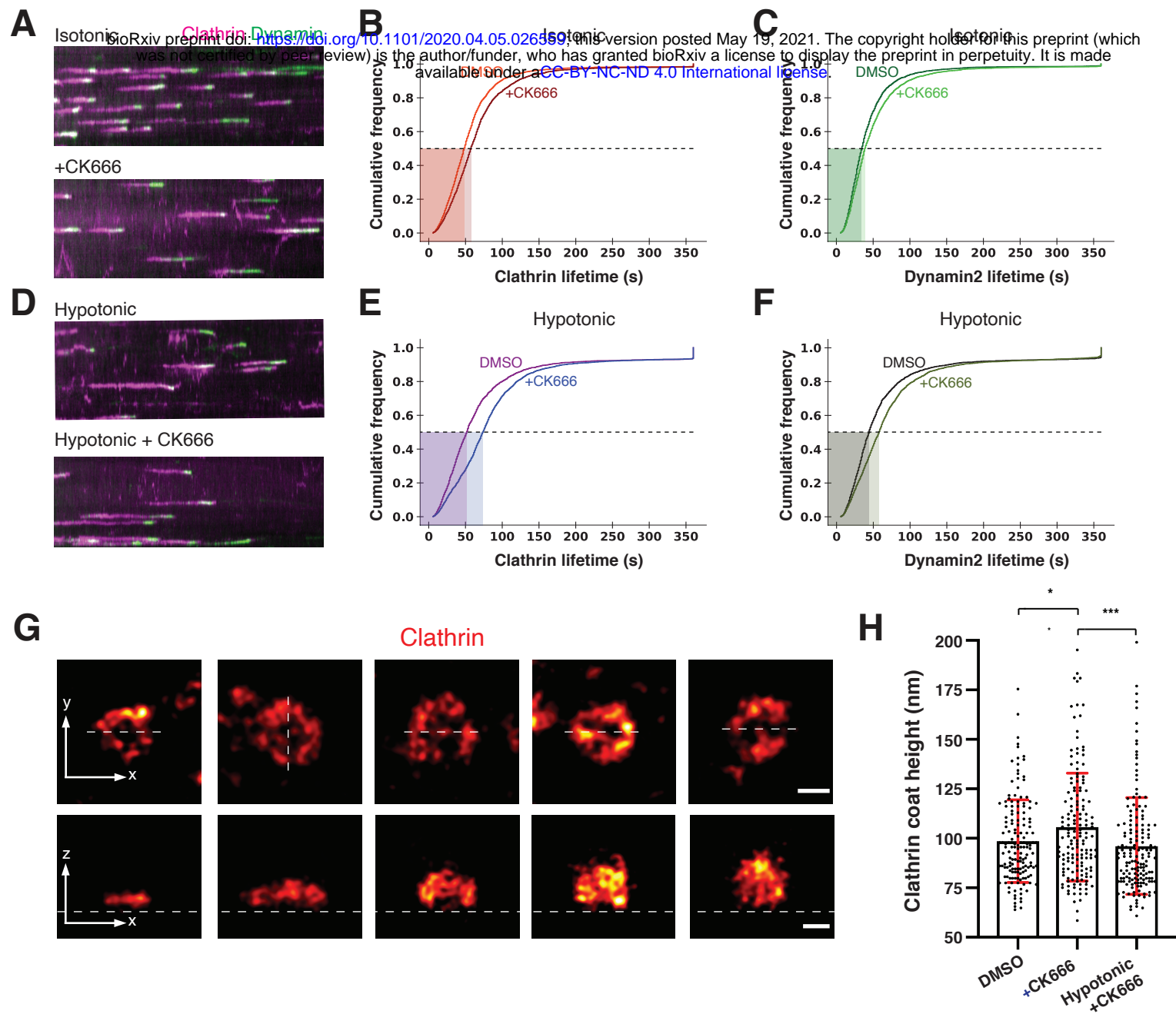
Figure 4: The actin network at CME sites increases in size in response to elevated membrane tension. In this figure, hypotonic refers to 75 mOsm media. (A) Schematic of cells in hypotonic media, which increases plasma membrane tension. The response of the actin network (blue) to elevated plasma membrane tension (purple) was previously unknown. (B) Representative STORM images of clathrin (red) and actin (cyan) in x-z projections for cells fixed after treatment in the hypotonic media for 5 min (bottom). Coated pits are classified as shallow, U-shaped, or omega-shaped based on the aspect ratio of the coat. Scale bars: 100 nm. (C) Plots of actin Z height at clathrin-coated pits from cells in the isotonic (n = 736) and hypotonic (n = 527) media measured from STORM x-z projections. Lines are median \pm interquartile range. $p < 0.0001$ determined by Mann-Whitney test. (D) Plots of actin coverage over the clathrin coat in pits found in STORM x-z projection images in isotonic (n = 719) and hypotonic (n = 509) conditions. Pits with actin coverage $> 1\%$ are plotted. Lines are median \pm interquartile range. $p < 0.0001$ determined by Mann-Whitney test. (E) Actin Z height as a function of coat shape in isotonic (gray, n = 736) and

hypotonic (purple, $n = 527$) conditions. **(F)** Actin Z height as a function of actin coverage over the clathrin coat in isotonic (gray, $n = 719$) and hypotonic (purple, $n = 509$) conditions. The data for isotonic conditions were also used to generate the plots in Figure 1. Three independent STORM experiments with $N_{\text{cells}} = 6$ in isotonic and $N_{\text{cells}} = 7$ in hypotonic media. **(G)** Cartoon depicting an adaptive actin force-generating mechanism that counteracts elevated membrane tension to ensure robust CME progression. This schematic describes three scenarios in which membrane tension is low, intermediate or high, and how CME is accomplished efficiently by adaptive actin network organization. Under low tension (bottom), the clathrin coat provides sufficient force to advance CME. At intermediate tension (middle), actin polymerization is required for the transition from U to omega shape. At high tension (top), endocytic progression slows. In the absence of actin polymerization, pits may stall at the shallow conformation. In response, the actin network grows to envelop the coat and provide additional force against high membrane tension. Arrows indicate actin forces exerted orthogonal and parallel to the membrane invagination.

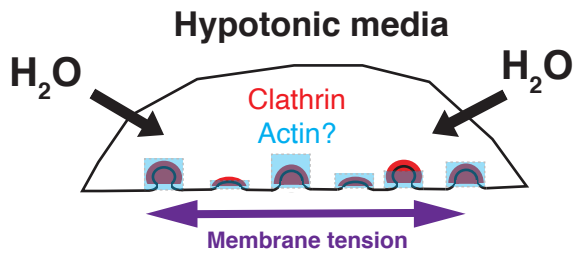
Figure 1



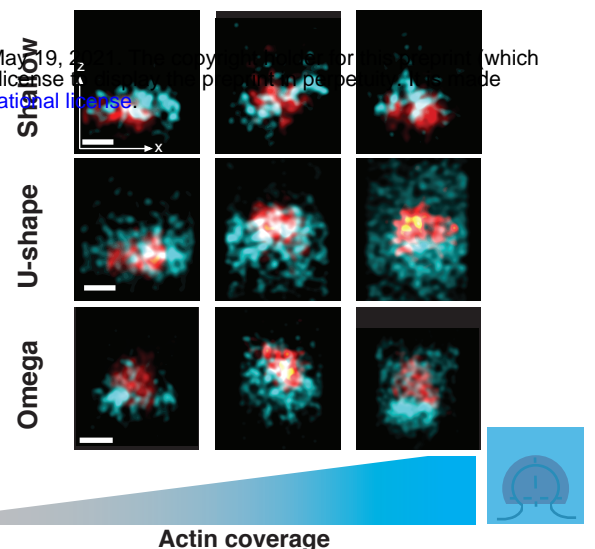
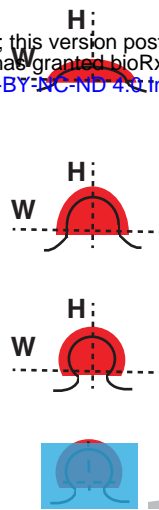




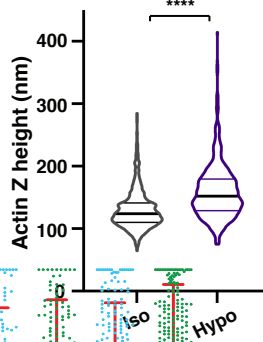
A



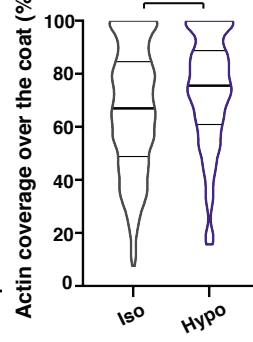
B



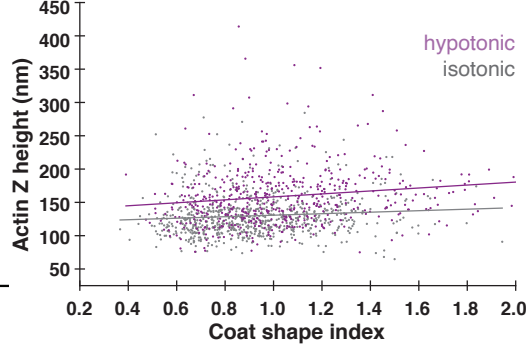
C



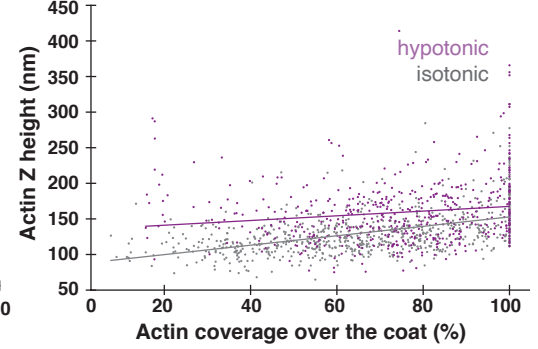
D



E



F



G

